Direct Inkjet 3D Printing Microwires with Small Feature Size by Freezing, Sublimation, and Evaporation Induced Colloidal Nanoparticles Self-Assembly Mechanism

Hao Guo, Lilan Zhao, Bo Qian, Qixin Wu, Rui Wang, Tianxiang Hua, Jing Qin, Lingying Li and Xuejun Shi*

Hao Guo, Bo Qian, Rui Wang, Lingying Li

Key Laboratory of Multifunctional Nanomaterials and Smart Systems, Suzhou Institute of Nano-Tech and Nano-Bionics, Chinese Academy of Sciences, Suzhou 215123, China;

E-mail: bqian2010@sinano.ac.cn

Lilan Zhao, Qixin Wu, Tianxiang Hua, Jing Qin

School of Nano Technology and Nano Bionics, University of Science and Technology of China, Suzhou 215123, China;

Xuejun Shi

School of Physical Science and Technology, Soochow University, Suzhou 215006, China;

Key words: inkjet 3D printing; small feature size; sublimation; colloidal nanoparticles; FSE-INS mechanism

Abstract

The feature size (FS) of inkjet printing is limited by nozzle size and drop spreading, which limits the realization of small optoelectronics devices and 3D microstructures. Some methods can realize small FS, but sacrifice advantages of inkjet technology. For instance, dewetting can reduce FS with all the advantages of inkjet technology kept, but is hard to print wires due to Rayleigh-Plateau instability. To solve these problems, in this paper, we introduced freezing and sublimation to direct inkjet printing wire processes. After optimizing the glycerol amount and adding tert-butyl alcohol (TBA) in water-based nanoparticle inks, condensed microwires of PS colloidal nanoparticles, graphene oxide (GO) nanosheets, and silver nanowires (AgNws) with small FS can be printed, respectively, by freezing, sublimation, and evaporation induced

nanoparticle self-assembly (FSE-INS) mechanism. Using printhead with the nozzle size of 21 μm, the minimum feature size is only about 2 μm for GO nanosheet samples. The FSE-INS mechanism shows particle-dimension dependent structure properties, introduces an additional particle manipulation freedom perpendicular to the substrate with sacrificial vertical solid surfaces, and exhibits great potential to realize small and novel devices and 3D structures, without sacrificing the advantages of inkjet technology.

1. Introduction

As an additive, high-throughput, multi-material, low-cost, and digital technology, inkjet printing has shown many advantages in the manufacture of optoelectronics devices and 3D structures. [1] However, the feature size (FS) of inkjet printing is limited by nozzle size and drop spreading,[2] which limits the miniaturization of printed functional devices and 3D structures. Some indirect ways like hydrophilic and hydrophobic pattern confinement[3] or guided methods[3b] have successfully realized wires with extreme small FS, but sacrificed the digital advantage, which may be the most important advantage of inkjet technology. Another indirect inkjet printing method modified jetting by satellite drops with the minimum diameter of 2.3 μm, [4] which is also very promising to achieve small FS. However, the method sacrificed the high-throughput advantage with a gas flow satellite drop manipulation system. Similar sacrifice can also be found in E-jet technology.[5] If keeping all the advantages of direct inkjet technology, dewetting is presently the only choice to achieve small FS.[6] But it is only good at printing dots, not wires, due to the surface tension induced Rayleigh-Plateau instability during shrinking.[7] There is only one report to print wires by dewetting with FS of 20 μm, but needed unique ink-substrate combination.[8] Even solute concentration variation will break the wires. Such small working window has already lost the multi-material advantage of inkjet technology. Due to these miscellaneous problems, the practical applications still need new mechanism for direct printing with small FS, and keeping all advantages of inkjet technology as much as possible.

In this paper, we introduced freezing and sublimation to direct inkjet printing processes to explore a new mechanism to realize small FS. Freezing is a natural process to inhibit drop spreading and Rayleigh-Plateau instability for water-based inks. As a possible origin of life,

freezing can concentrate suspensions in micro-channels between ice crystals, which is very different from evaporation induced concentration.[9] Sublimation has self-similar smoothing shrinking effect.[10] PS colloidal nanoparticles, graphene oxide (GO) nanosheets and silver nanowires (AgNws) were chosen as the research representatives for 3D, 2D, and 1D nanoparticles, respectively.

Tert-butyl alcohol (TBA), as one of the few water co-solvent employed in the freeze-drying of commercially available pharmaceutical products, was added into the inks to adjust the rheological properties[11] to achieve stable jetting. TBA also can form small needle-like ice crystals with water[12] to reduce the distances between the concentrated suspensions in micro-channels during freezing, which increase the opportunity for the merging of the released concentrated suspensions during sublimation. Glycerol, as a common cryoprotectant in low-temperature biomedical technology, can significantly inhibit the growth of ice crystals.[13] It was added into the inks to contribute unfrozen liquid bridges for the merging of the concentrated suspensions and condensation of the final structures. Since the liquid bridges should be volume comparable with nanoparticles, the amount of glycerol in inks was also volume comparable with the total volume of nanoparticles.

After optimization of the glycerol amount and print conditions, the condensed PS nanoparticles, GO nanosheets, AgNws microwires with small FS were finally prepared, respectively, by freezing, sublimation, and evaporation induced nanoparticle self-assembly (FSE-INS) mechanism as shown in Figure 1. The minimum FS of the microwires is only about 2 μm for GO nanosheets, which is about 1/10 of the nozzle size. The FSE-INS mechanism shows particle-dimension dependent wires' height-width ratio and particles' arrangement in the wires, and exhibits great potential to fabricate small and novel devices and 3D structures.

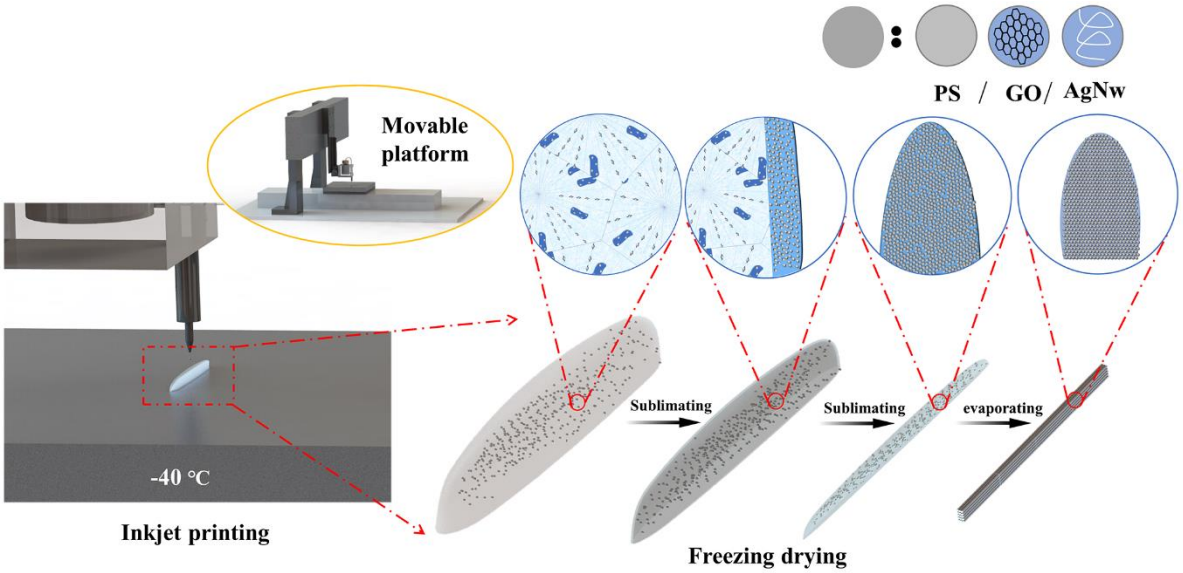

Figure 1. Schematics of printing processes. From left to right, the processes including freezing inkjet drops on -40 °C substrate; then, sublimation of the ice crystals in frozen structure with the structure shrinking; finally, evaporation of the residual liquid in the remain structure by vacuum-drying. The circular insets illustrated the microscopic evolution of the printed structure by FSE-INS mechanism, which will be discussed in the following sessions in details.

2. Results and Discussion

2.1. Freezing the jetting drops

To achieve stable jetting, the dimensionless number Ohnesorge number (Oh) of ink is a key criterion, which is derived from the other two dimensionless numbers including Reynolds number (Re) and Weber number (We) [2]:

$$Re = \frac{v\rho a}{\eta} \tag{1}$$

$$We = \frac{v^2 \rho a}{\gamma} \tag{2}$$

$$Oh = \frac{\sqrt{We}}{\mathrm{Re}} = \frac{\eta}{(\gamma \rho a)^{1/2}} \tag{3}$$

Where, v (m s^{-1}) is the drop velocity, η (mPa s) is the viscosity, γ (mN m^{-1}) is the surface tension, ρ (g ml^{-3}) is the density, and a (μm) is the nozzle diameter.

The inverse of Oh, $Z = 1/Oh$ is suggested to characterize drop formation: When $10 > Z > 1$, usually stable inkjet droplets can be formed. Z values for PS+G1.2, GO+G1.8, and

AgNws+G0.4 inks (sees the ink naming rule in Experimental: Ink Preparation section) were calculated as Z_{PS} = 7.25, Z_{GO} = 6.82, Z_{AgNws} = 9.78, which are all in the stable jetting region. Note that since glycerol is a small amount additive with volume comparable with the total volume of nanoparticles, the amount variation of glycerol in PS and GO inks has no big influence on *Z* as well as the jetting properties. It is also worth to note that since fluid will suffer high shear force at the orifice of printhead, and both GO and AgNws inks are pseudoplastic fluids as shown in Figure S1b, the viscosities at high shear rate of all the three kinds of inks were used for *Oh* calculations. Note that since there is no big difference of the general structure morphologies printed by the inks with different kinds of nanoparticles during freezing and most period of sublimation due to the small nanoparticle volume ratios in the inks, PS+G1.2 ink was chosen as the representative to illustrate the whole printing processes.

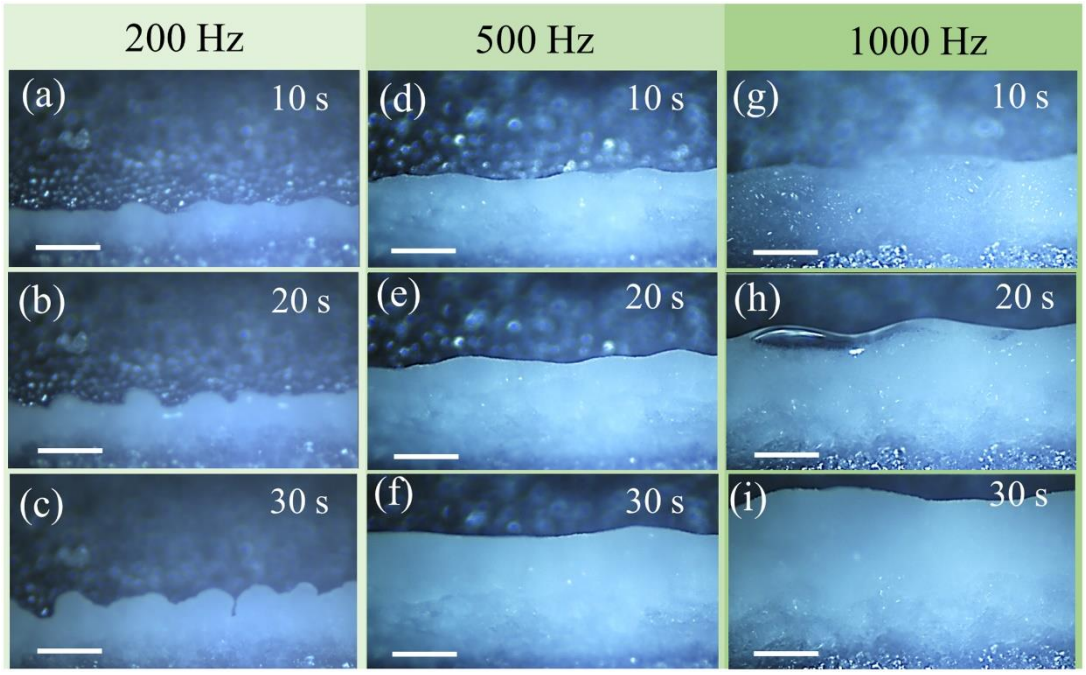

Figure 2. Drop frozen and accumulation images of PS+G1.2 ink with print frequency of (a-c) 200 Hz, (e-f) 500 Hz, and (g-j) 1000 Hz at 10s, 20s, and 30s, respectively. The scale bar is 100 μm.

Figure 2 shows the drop frozen and accumulation images during wire printing at frequencies of 200 Hz, 500 Hz, and 1000 Hz, respectively. Each wire was printed by 20 passes on -40 ℃ silicon (001) substrate, and intentionally without special (hydrophobic) treatment. To create

enough room for imaging, a microfab printhead was used only in Figure 2 as a replacement of the real print process by the dimatix printhead with the same distance between the nozzle and substrate of 2 mm. Note that a little difference of the nozzle size between the microfab (30 μm) and dimatix (21 μm) printheads has no big influence on the droplet impingement and coalescence processes.

It can be observed in Figure 2 and Video S1 that the drops were rapidly frozen in sequence along the print direction on substrate at the first print pass, and accumulated layer by layer at the successive passes. The initial freezing event limited the droplet spreading as well as the width of the printed wire. After hitting on the substrate, it took a short time for the droplets oscillation before being frozen as shown in Video S1, which gave the droplets a limited time to flow. The relation between the neighbor printing droplet spacing (PDS) d (μm), the printhead moving speed v (μm s^{-1}) and the print frequency f (Hz) is calculated by equation 4:

$$d = v/f \tag{4}$$

According to equation 4, when f increasing with same v, d will decrease. Comparing with f, d is a more straightforward parameter to understand the drop accumulation process. Note that v is 10^4 μm s^{-1}. Then, the corresponding d at 200Hz, 500Hz and 1000Hz are 50 μm, 20 μm and 10 μm, respectively. The widths and heights of the wires printed at d of 50 μm, 20 μm and 10 μm are estimated in Figure S5, which are about 100μm*200μm, 150μm*300μm and 200μm*500μm, respectively. Generally, when d decreasing, the width of the printed wire is increasing, which is due to more drops accumulated within unit length. The surface roughness of the wires at d of 50 μm is higher than that at 20 μm and 10 μm, which is due to insufficient drops at large d.

The droplet impingement, solidification and accumulation in Figure 2 and Video S1 were complex physical processes driven by inertial forces, capillary forces and gravity[14]. To better understand these physical processes, the sequence of events and temperature distributions after the droplets impact and accumulation on -40 °C substrate with 500 Hz jetting frequency were simulated as shown in Figure 3. The viscosity and surface tension were derived from PS+G1.2 ink. The simulation model parameters and control equations are in the supplementary material. In Figure 3, generally, the temperature distribution close to the substrate is symmetric and

substantially tailored by the center droplet flighting trace. In Figure 3a, when approaching the substrate, the first droplet rapidly raises the temperature of the space points on the flighting trace, then the temperature of the regions surrounding the flighting trace by heat transfer. After impacting on the substrate as shown in Figure 3b, the droplet starts to diffuse and oscillate under the action of inertia force, viscous force, and surface tension, with the temperature of the regions along and surrounding the flighting trace gradually decreasing. Then, in Figure 3c, the droplet continues to finitely spread for 15 μs with its temperature fast decreasing to < 0 °C and the temperature of the regions along and surrounding the flighting trace continuing to gradually decrease. Finally, in Figure 3d, after fast retracting and oscillation processes dominated by surface tension for about 200 μs, the droplet reaches a stable state, with the temperature of regions close to the substrate decreasing to about -40 °C, including the droplet. The second droplet then diffuses, oscillates, and rebounds to a stable state covering the first droplet as shown in Figure 3e-h with the temperature evolution from approaching to the substrate to stable state is almost same with that of the first one. It can be observed that the heat carried by the second droplet will melt and merge with the top part of the first solidified droplet, which leads the lateral size increasing. Continue to accumulate the droplets, the height of the frozen structure grows, while the lateral size approaches to a fixed value as shown in Figure 3i-l. Such anisotropic structure accumulation process on freezing substrate is supposed to benefit to the lateral size control of the print structure.

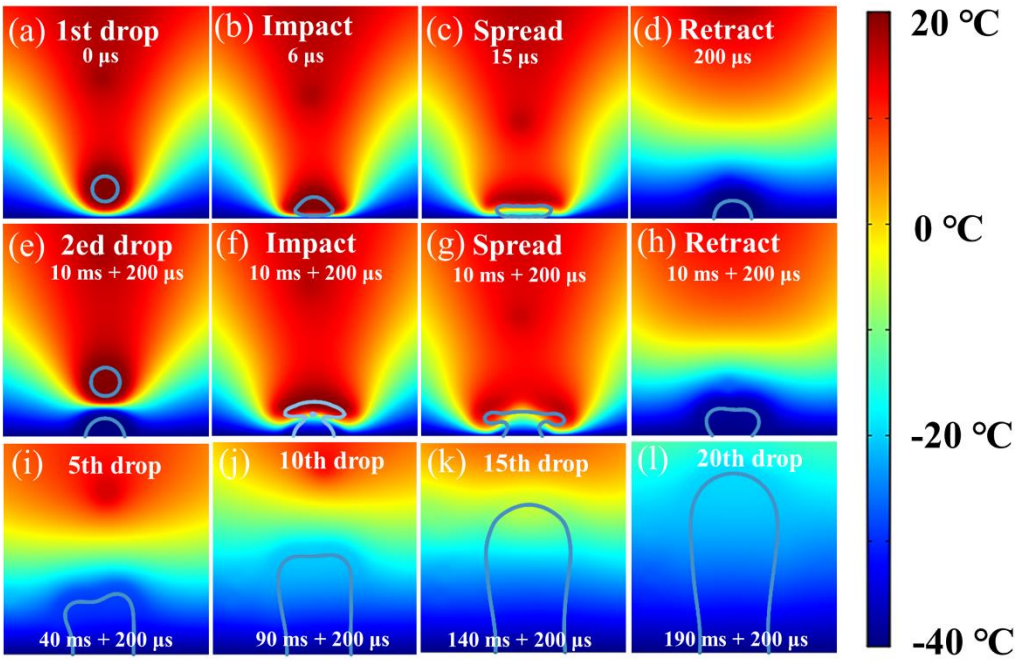

Figure 3. Simulation of the sequence of events and temperature distributions after the droplets impact and accumulation on -40 °C substrate. The first droplet (a) approaches, (b) impacts, (c) spreads, and (d) retracts on substrate. The second droplet (e) approaches, (f) impacts, (g) spreads, and (h) retracts on the frozen structure of the first droplet. The accumulation of the (i) 5^{th}, (j) 10^{th}, (k) 15^{th}, and (l) 20^{th} droplets.

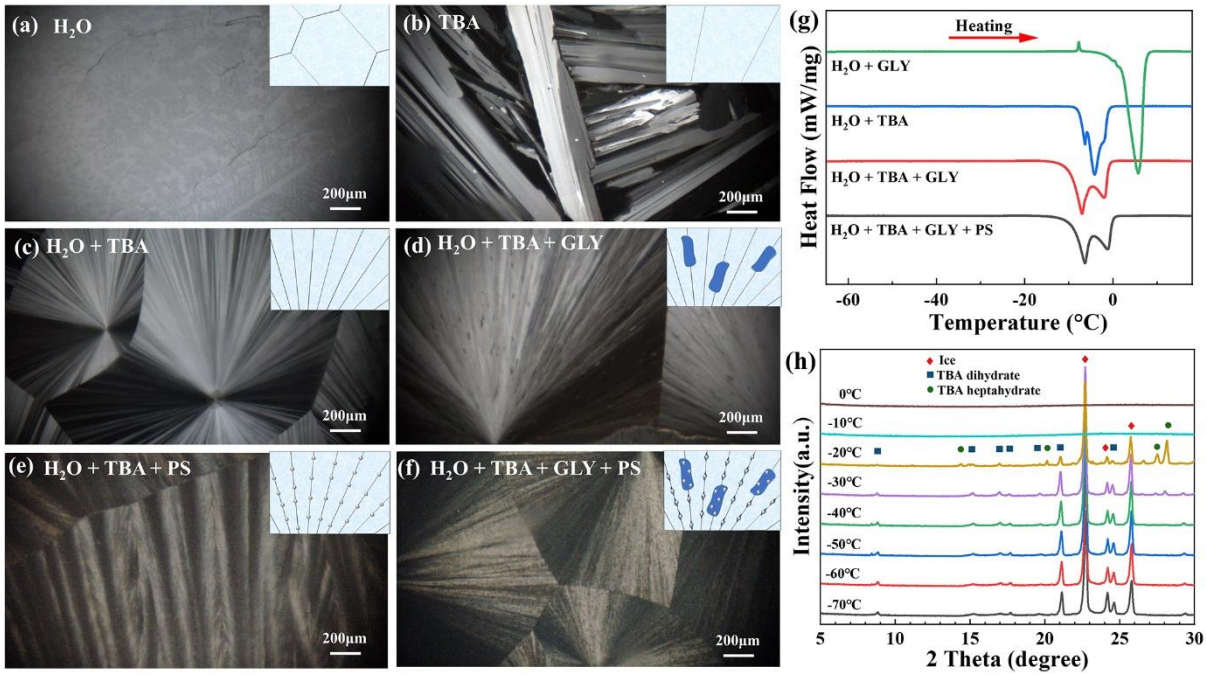

Figure 4. Polarizing microscope images and summarized solid/liquid distribution inset images of different frozen mixtures of the components of PS+G1.2 ink: (a)Water (H_2O); (b) TBA; (c)

H_2O and TBA; (d) H_2O, TBA and glycerol (GLY); (e) H_2O, TBA and PS nanoparticles (PS); (f) H_2O, TBA, GLY and PS; (g) DSC heating curves of different frozen mixtures of the components of PS+G1.2 ink. (h) Low temperature XRD patterns of frozen PS+G1.2 ink.

The polarizing microscopic images of the different frozen mixtures at -40 °C of the components of PS+ G1.2 ink are shown in Figure 4a-f with the insets presenting the summarized solid/liquid distribution images. It can be observed that the frozen crystals can be easily modified from big ice crystals of water in Figure 4a, and discontinuous big rodlike crystals of TBA in Figure 4b, to small needle-like crystals of the water-TBA mixture in Figure 4c. After adding small amount glycerol into the water-TBA mixture, many anisotropic small dark dots between the needle-like crystals appears in Figure 4d. The long axes of these anisotropic dots are along boundaries of the crystals. Since the ice crystals growth during freezing has repelling and concentration effect on the unfrozen substances just like the freezing of sea water, and glycerol has a critical concentration of 40 mol% in frozen water-based solution,[15] the dark dots in Figure 4d should be glycerol-water mixture. After adding PS nanoparticles into water-TBA mixture, the boundaries of the crystals become blurry as shown in Figure 4e. However, the boundaries of the crystals in Figure 4f of PS+G1.2 ink are clearer than that in Figure 4e, and similar with Figure 4d, which is due to the different thermal conductivity of nanoparticles[16] and glycerol affecting the local ice crystals morphology and growth kinetics, especially at the boundaries. This also indicates that for PS+G1.2 ink, PS nanoparticles were always encapsulated with glycerol-water mixture in the micro-channels between ice crystals, and had few opportunities to be encapsulated alone. Between the ice crystals in Figure 4f, there are more, smaller, and more evenly distributed anisotropic dark dots than those in Figure 4d, which indicates the concentrated PS nanoparticle suspensions hard to be merged between ice crystals due to higher viscosity. Note that the polarizing microscope images of the frozen structures of GO+G1.8 and AgNws+G0.4 inks in Figure S12 show similar small and evenly distributed anisotropic dark dots with those of PS+G1.2. This indicates the local ice crystals morphology and growth kinetics are mainly affected by glycerol for the inks with different kinds of nanoparticles. It is also worth to note that since the freezing process for the polarizing

microscopy measurements in Figure 4 was a static process, while the jetting drops on the substrate during printing experienced many instant events including oscillation, melting, and refreezing, etc., as shown in Figure 3, the concentrated suspensions distributions in the printed structures should be a little different from the results in Figure 4f and S14, respectively.

Figure 4g shows the differential scanning calorimetry (DSC) heating curves of different frozen mixtures of the components of PS+G1.2 ink. All the peaks of the curves locate in the range from -20 to 10 ℃. For the mixture of glycerol-water, there is one big endothermic peak at ~5.74 ℃. For the mixture of TBA-water, three endothermic peaks with the positions close to each other can be observed: the two sharp peaks in the range from -7 to -3 ℃ is due to the eutectic melting of TBA hydrate phase; while the one at about -2.1 ℃ is attributed to the melting of ice[17]. For water-TBA-glycerol mixtures, small amount glycerol did not raise the melting temperature comparing with the curve of water-TBA mixtures, but generated two clear separated endothermic peaks at -6.9 ℃ and -1.9 ℃, covering a broader range, which are related to the melting of TBA hydrate eutectic and ice, respectively. The broaden peak range indicate that metastable TBA hydrate phases exists in the system.[18] After adding PS nanoparticles to water-TBA-glycerol mixtures, the two endothermic peaks similar with those for glycerol-TBA-water mixture can be observed, except a little bit broadening. It means PS nanoparticles had no big influence on the system except introducing a little bit more defects as well as amorphous phases on the ice crystals boundaries as shown in Figure 4f. Similar endothermic peaks can be expected when adding GO nanosheets or AgNws due to the similar morphologies in Figure 4f and Figure S12.

The evolution of the crystalline phases frozen from PS+G1.2 ink was measured by in-situ low temperature XRD in Figure 5b. At -70 °C, three characteristic peaks of ice of water (22.7, 24.2 and 25.7° 2θ) are observed, and the crystallization peaks of TBA dihydrate appear at 8.8, 15.2, 17.0, 21.1 and 24.5° 2θ. The peak shape is almost unchanged from -70 to -30 ℃. At -20 ℃, the peaks intensity of TBA dihydrate decreases with the emergence of the crystallization peaks of TBA heptahydrate at 14.4, 20.1, 27.6 and 28.2° 2θ.[17] All peaks disappear at -10 ℃. The results indicate the complexity of the TBA related ice crystals in the frozen structures.

Note that the print substrate temperature -40 ℃ is much lower than the phase transition temperature in Figure 4g-h, which indicates for the drops approaching the substrate, the cooling speed was very fast, which drove the system far from equilibrium. Once nucleation occurred, the growth of ice crystals was explosive, which resulted in quick fixing the printed structure as shown in Figure 2 and Video S1.

2.2. Ice crystals sublimation

After freezing process, to release the concentrated nanoparticle suspensions between ice crystals without dilution, sublimation of ice crystals is an inevitable process. Figure 5 illustrates the microscopic morphology evolutions of the wires printed by PS+G1.2 ink (Figure 5a-f) and its solvent (Figure 5g-l) during ice crystals sublimation with 15 second intervals, respectively. In Figure 5a-f, with time increasing, the rough wire with the width of about 150 μm gradually shrank to uniform smooth fine wire with the width of about 20 μm even on ordinary substrate, and with some residuals close to the wire. In Figure 5g-l, the wire with the width of about 150 μm shrank to discontinuous fine smooth wire with the width of about 20 μm on a clean substrate. The results mean the sublimation of ice crystals can significantly reduce the width of printed wire on the substrate without special treatment, while Rayleigh-Plateau instability was efficiently inhibited for the wire composed of concentrated nanoparticle suspensions during shrinking. Note that the small substances covering all over the substrate at the beginning of sublimation in Figure 5a-g are ice crystals frozen from water in air, and can be easily sublimated as shown in Figure 5b-f and 5h-l.

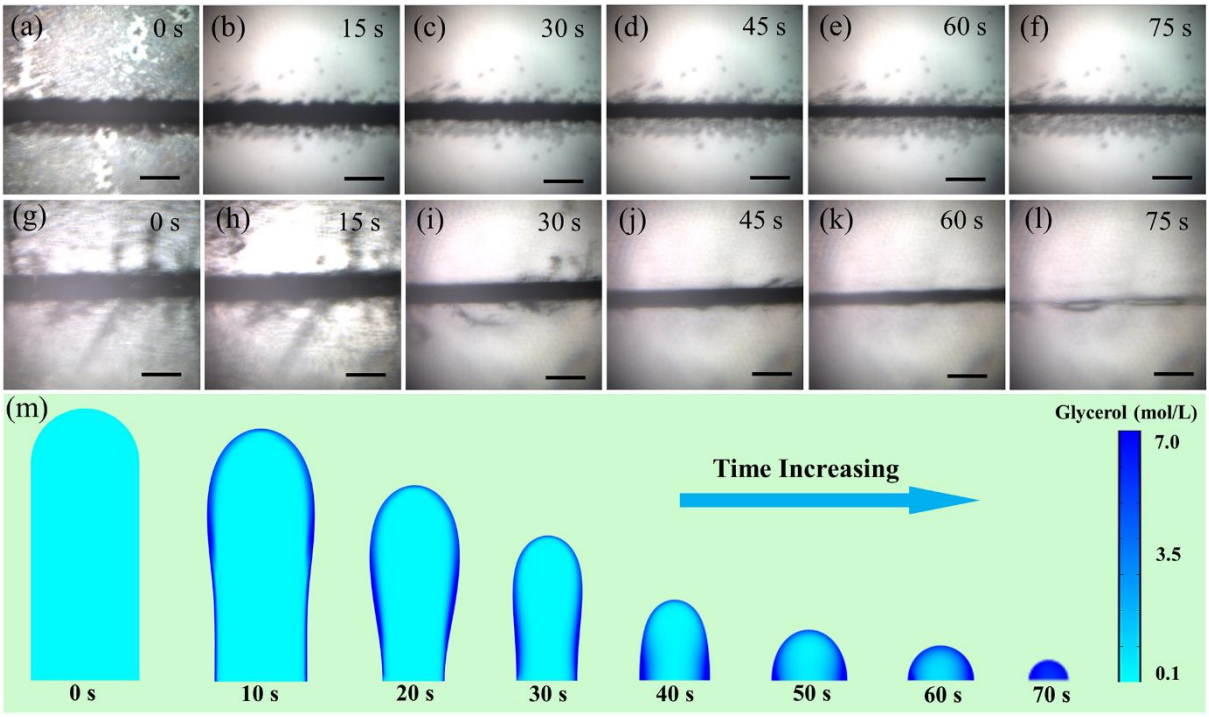

Figure 5. The microscopic morphology during sublimation of the wires printed by (a-f) PS+G1.2 ink, and (g-l) its solvent at 15 s intervals, respectively. The scale bar is 200 μm. (m) Simulation of the sublimation process of the droplet accumulated frozen structure of the solvent of PS+G1.2 ink.

The mass (m) loss of ice crystals during sublimation was the main reason of the shrinkage, and was governed by the rate of the mass transfer[10a]:

$$h \cdot \Delta T = \frac{\partial}{\partial t} m \cdot \frac{\Delta H_{sub}}{M_w} \tag{5}$$

where h is the heat transfer coefficient of the system and ΔT is the temperature difference between the environment and sample. Assuming the environment temperature is constant (ΔT is constant), both h and the sublimation latent heat ΔH_{sub} are constants, the equation reveals the change in the printed structure volume ΔV, is proportional to the change in time Δt. In details, the sublimation of ice drop can be described by the coupling system of equations:[10b]

$$\nabla^2 \rho(r) = 0, \qquad \rho|_{r=\Omega} = \rho_{sat}(T_s), \qquad \rho|_{r=\infty} = \rho_\infty \tag{6}$$

$$v_n \equiv j_n = -\frac{D}{\rho_{ice}} \mathrm{n} \cdot \nabla \rho(r)|_{r=\Omega} \tag{7}$$

Where ρ is the vapor mass concentration, which diffuses with a constant diffusion coefficient D from its (constant) saturation value ρ_{sat} at the ice surface to a fixed (lower) value ρ_∞ far

away from the ice. ρ_{ice} is the ice density, Ω is the solid boundary whose outward normal is n. v_n and j_n are the diffusion speed and local flux of the interface, respectively, in the normal direction. Since Equation (6) is Laplace's equation, the diffusion problem for $\rho(r)$ is mathematically equivalent to the electric potential around a charged conductor. It means the sublimation of ice has strong curvature dependence which is analogous to the known electrostatic tip effect, and consistent with the wire morphology evolutions from rough to smooth in Figure 5a-f and 5g-l.

To understand the release process of the concentrated suspensions, a simplified model of glycerol concentration evolution in drop accumulated frozen structure during sublimation was simulated in Figure 5m, due to glycerol-water mixture always encapsulated with PS nanoparticles and playing a main role on the local ice crystals morphology as analyzed from Figure 4d-f and S14. The initial structure in Figure 5m is similar with that in Figure 3l. In Figure 5m, the glycerol-water mixtures are gradually released and accumulated by capillary force along the surface of the shrinking frozen structure with ice crystals sublimated from outside to inside. The released liquid tends to flow downward due to the surface tension and gravity, but very slow due to the high viscosity of glycerol. The shrinking frozen structure acts as a sacrificial template carrying the continuously released liquid on its moving surface to converge and accumulate into a small drop when all the ice crystals vanish, with the drop size determined by the volume of glycerol. The accumulation of most part of liquid is substrate independent due to different space, except the part contacted with substrate, which was simplified in the simulation. If nanoparticles are introduced in this system, the concentrated nanoparticle suspensions between the ice crystals will also be gradually released and accumulated along the surface of the shrinking frozen structure during sublimation until the ice crystals vanish. Since the nanoparticles are volume comparable glycerol, the structure accumulated with high viscosity concentrated suspensions after sublimation can be considered as a wet granular pile[19] with almost close-packed nanoparticles connected by capillary liquid bridges, and not a pure liquid drop in Figure 5m. The high viscous concentrated suspensions and sacrificial ice template are the main factors against Rayleigh-Plateau instability during shrinking as shown in Figure 5a-f. Note that evaporation will also happen during sublimation for the released suspensions.

Due to the lower boiling point and the short sublimation time, the most likely fast evaporation liquid during sublimation is water,[20] which will make the released suspensions more concentrated and viscous.

2.3. Evaporation induced condensation

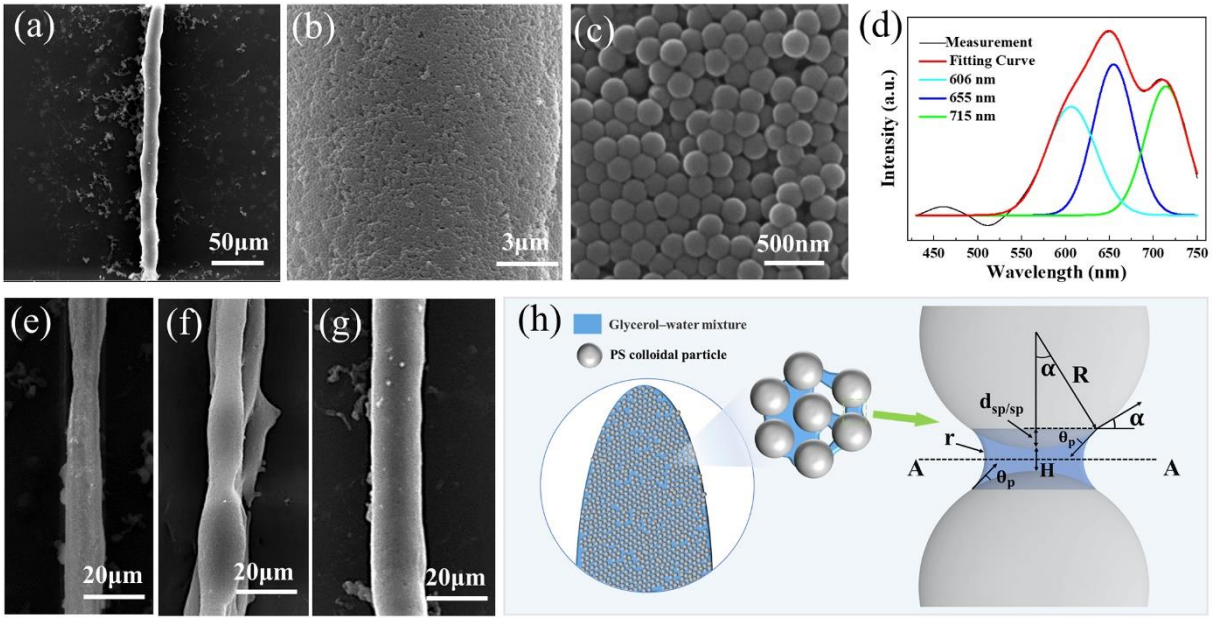

Figure 6. (a-c) SEM images and (d) micro-reflectance spectra of the PS wires printed by PS+G1.2 ink with PDS of 10 μm. The SEM images of PS wires printed with PDS of (e) 50 μm, (f) 20 μm, and (g) 10 μm. (h) Schematics of evaporation-induced PS nanoparticles self-assembly mechanism.

After the residual liquid exhausted by evaporation, the wet granules turned into condensed microwires. In Figure 6a, the PS wire shrinks densely to the width of about 20 μm, with a little bit periodic irregularity on both sides, which indicates Rayleigh-Plateau instability still had a little bit influence on the released suspensions during the wire shrinking although being largely inhibited by high viscous liquid and ice crystals template. In Figure 6b and c, the wire surface is smooth with close-assembled PS nanoparticles with random arranged hexagonal, face-centered cubic and cavitation structures. This can be confirmed by the micro-reflectance spectroscopy in Figure 6d. There are three Gaussian fitting peaks at around 610 nm (cyan), 655 nm (blue), and 720 nm (green). The green and blue peaks are possibly related to the long- and

short-range order amorphous photonic crystals arrangement of PS nanoparticles, respectively; while the cyan peak is possibly related to the materials surface reflection. [15a, 21] Figure 6e-g show the PS wires printed with different PDS. The morphologies of the wires change from narrow, rough, and bulging instable with PDS of 50 μm, to wider, smooth, and bulging instable with PDS of 20 μm, then to the widest, smooth, and close to parallel-sided except a little bit irregularity with PDS of 10 μm. There are residual nanoparticles close to the printed wires on the substrate in Figure 6a and e-g, which has been observed in Figure 5f. These are the drag footprints by capillary force of the released concentrated suspensions on the shrinking surface and contacted with the substrate during sublimation, which can be eliminated by hydrophobic substrate as shown in Figure S10. The residual nanoparticles are minority, most of the nanoparticles are not influenced by substrate. In Figure S7, the height of the PS wire printed with PDS of 20 μm is measured about 50 μm, which is larger than the width of about 15 μm in Figure 6f. This means the wire inherits the anisotropic property of the frozen structure with large height-width ratio of about 3.3. The corrugated side morphology of the wire in Figure S7 was mainly defined by the drop flow before being frozen as shown in Video 1, which is common for drop accumulation 3D printing technology.[22]

Figure 6h illustrates the schematics of evaporation-induced PS nanoparticles self-assembly mechanism. The final evaporation process starts from the wet granular pile after sublimation. Glycerol-water mixtures act as liquid bridges to gradually pull PS nanoparticles closer to each other by capillary traction force during the evaporation. The capillary force can be expressed as:[23]

$$F_{capillary} = 2\pi\gamma R \sin\alpha \sin(\alpha+\theta) + 2\pi\gamma R\cos\theta/[1+H/2d] \quad (8)$$

Where α is the half-filling angle, γ is the surface tension of the liquid, θ is the liquid–solid contact angle, R is the sphere radius, H is the shortest distance between the spheres; d is the immersion length of the sphere and calculated by $d = (H/2) \times \left[-1+\sqrt{1+2V/(\pi\alpha H^2)}\right]$, where V is the volume of liquid bridge. H are gradually reduced by the capillary traction force until all the liquid exhausted and final condensed PS structure forms.

Note that the results in Figure 6 have been optimized by tuning the amount of glycerol. Less glycerol made the released concentrated PS suspensions during sublimation too viscous to flow

on the shrinking surface, and have fewer opportunity to be fully merged, which led to porous and discontinuous structures, and with more residual nanoparticles as shown in Figure S6a-c and S6e-g, respectively. On the contrary, too much glycerol made the viscosity of the released concentrated PS suspensions during sublimation too low, which made the concentrated PS suspensions very easily flow and spread without any shrinking effect as shown in Figure S6m-o.

2.4. Preparation and characterization of RGO wires

Similar with the PS wires, by tuning the concentration of glycerol as shown in Figure S8, the GO wires printed by GO+G1.8 ink with 20 passes in Figure 7a-f show the best morphologies. The GO wire in Figure 7a exhibits long, uniform, and condensed morphology with the width only about 2 μm, which is much narrower than that of the PS wires. By tuning PDS from 50 μm to 20 μm, then to 10 μm, the widths of the GO wires change from 2 μm to 3 μm, then to 5 μm, respectively, as shown in Figure 7b-d, which is similar with the width evolution of the PS wires in Figure 6e-g. However, the roughness of the GO wires increases with PDS decrease, which is contrary to the PDS dependent roughness evolution of the PS wires. The GO nanosheets are confirmed to be well assembled along the print direction and close packed in Figure 7e and f. Wrinkles can be observed on the surface, which were originated from the suspensions downward flow during freezing of jetting droplets and sublimation of ice, and shrinking during final evaporation. In Figure 7f, vertical oriented GO nanosheets can be observed on the cross-section. Since the original width of the frozen structure printed by GO+G1.8 ink is about 100 μm with PDS of 50 μm, the final GO wire show 50-fold shrinkage in width. Such large shrinkage ratio and nanosheet orientation of the GO wires indicate the contribution of the anisotropic feature of GO nanosheets.[24] In Figure 7h, the size of GO wire printed with PDS of 10 μm are about 3.9 μm for height, and 5 μm for width, which indicates the final GO wire inherited part of the anisotropic property of the initial frozen structure.

Tracing back the print processes, the GO suspensions were suddenly concentrated between the ice crystals as shown in Figure S12a after the ink drop hitting on the substrate. According to Onsager theory, [25] when the concentration increase, under the action of orientation entropy,

the isotropic distributed GO nanosheets will transfer into nematic liquid crystal with parallel orientated GO nanosheets. The critical theoretical volume fraction Φ for the transition between isotropic to nematic phases is calculated from equation 9 [26]:

$$\Phi = \frac{3}{8}\sqrt{3}\frac{L}{D}\frac{1+\sigma^2}{1+3\sigma^2}\rho D^3 \quad (9)$$

It was reported that dimensionless number density D^3 of isotropic and nematic transition concentrations were $D_{iso}{}^3 = 2.7$ and $D_{nem}{}^3 = 4.3$, respectively. The sheet thickness L was estimated to be 0.8 nm, the GO sheet density ρ was 2.2 g cm^{-3},[26] the sheet average lateral size D was 345 nm, and the polydispersity σ of the system was determined by dividing the standard deviation of diameter distribution (156 nm) by D. The above equation gave the biphasic region with the GO concentration between 3 to 14.6 mg mL^{-1}. The GO nanosheet distribution is isotropic in the range smaller than 3 mg mL^{-1}, and nematic in the range larger than 14.6 mg mL^{-1}. Considering the 40 mol% glycerol critical concentration in water after being frozen, the concentration of the GO suspensions encapsulated between the ice crystals can be calculated as 112.4 mg mL^{-1}, which is much larger than 14.6 mg mL^{-1} and means the concentrated GO nanosheet suspensions from GO+G1.8 ink are nematic liquid crystal with the parallel oriented GO nanosheets with the orientation parallel to the local ice/liquid interfaces as shown in Figure S12a.

Figure 7g illustrates the deductive schematics of the sublimation details of the frozen structure of GO ink according to the model in Figure 5m. The concentrated GO suspensions will be gradually released to the surface of the shrinking frozen structure during sublimation. The released oriented GO nanosheets tend to arrange parallel to the surface of the shrinking frozen structure by the liquid capillary traction force as shown in the upper inset of Figure 7g. Therefore, due to the ice template introducing surfaces perpendicular to the substrate, the GO nanosheets on these surfaces tend to arrange also perpendicular to the substrate as shown in the bottom inset of Figure 7g, which is consistent with the cross-section morphology in Figure 7f, although there are wrinkles introduced by freezing, sublimation and evaporation processes on side surfaces of the final structure. Also note that there are residual nanosheets close to the wires on the substrate in Figure 7a-d with the same reason as analyzed for PS wires, which can be efficiently eliminated by hydrophobic substrate as shown in Figure S10.

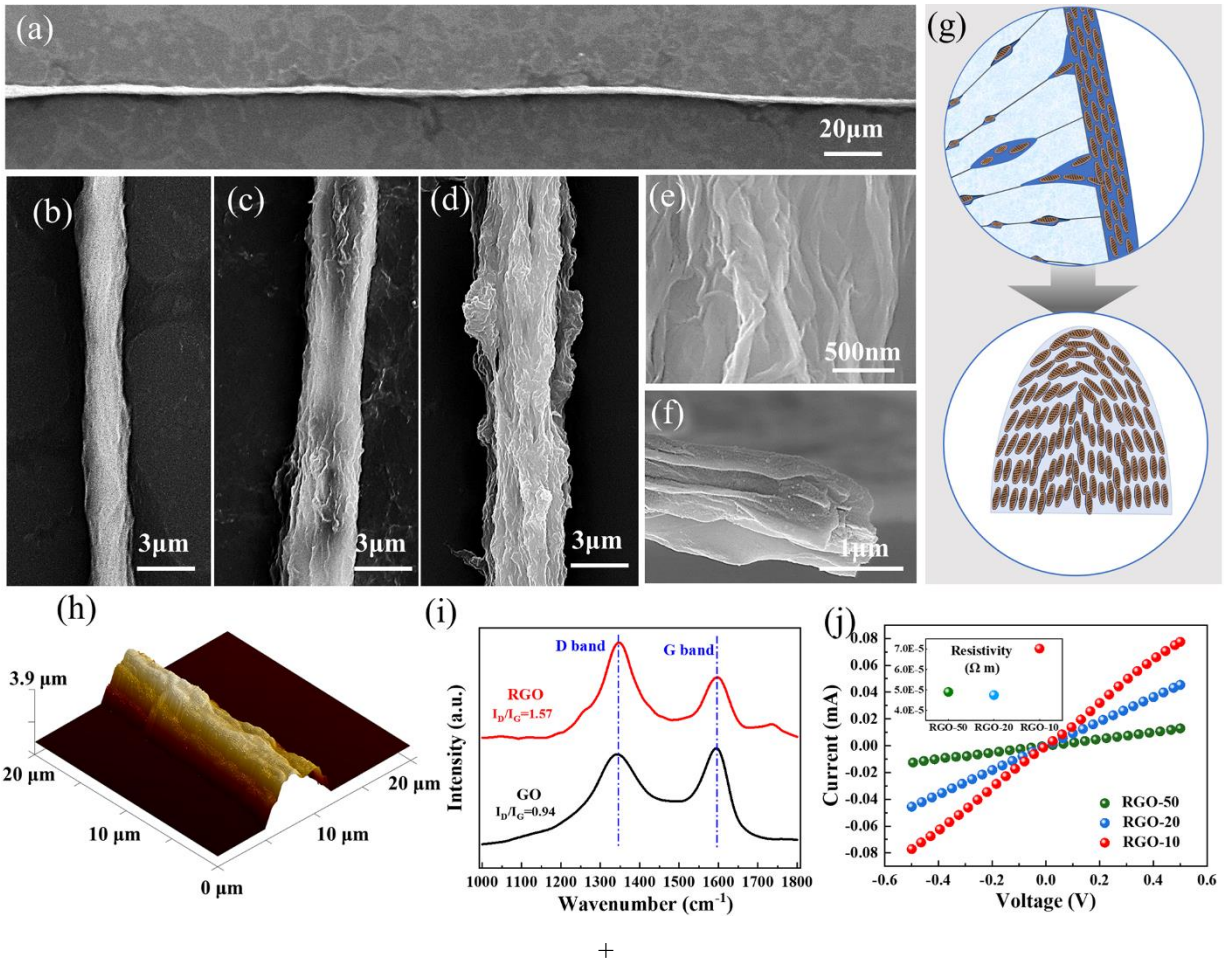

Figure 7. The properties of the wires printed by GO+1.8G. SEM images of GO wires with PDS of (a and b) 50 μm, (c and f) 20 μm and (d and e) 10 μm, respectively. (g) Deductive schematics of the release details of GO suspensions during sublimation. (h) AFM image of GO wire with 10 μm PDS. (i) Raman spectra of GO and RGO wires with 10 μm PDS. (j) I–V curves and resistivities of the printed RGO wires.

To study the electrical properties, the GO wires were reduced by a mixture of hydroiodic acid and glacial acetic acid[27]. The ratios of the peak intensities of D and G (I_D/I_G) of GO and RGO in the Raman spectra in Figure 7i are 0.94 and 1.57, respectively, which means the good reduction effect. The RGO wires printed with smaller PDS exhibits better conductivity as shown in the I-V curves in Figure 7j, which is consistent with the amount of the nanosheets in unit length. By calculation, the resistances per unit length of RGO-50 (50 μm PDS), RGO-20 (20 μm PDS) and RGO-10 (10 μm PDS) are 38.7, 11.0 and 6.3 kΩ mm^{-1}, respectively. The

resistivities calculated according to Equation S1 and the cross-sectional areas (Figure S14a) of RGO-50, RGO-20, and RGO-10 are 4.9×10^{-5} Ω m, 4.8×10^{-5} Ω m and 7.0×10^{-5} Ω m, respectively, which are low enough to be applied in microelectronic devices.

2.6. Preparation and characterization of AgNws wires

The AgNws properties printed by the optimized AgNws+G0.4 ink are illustrated in Figure 8. The AgNws wire printed with 10 μm PDS in Figure 8a is uniform but with bulging instability on both sides, and with the width of about 15 μm. In Figure 8b-d, with the PDS decrease from 50 μm to 20 μm, then to 10 μm, the wires becomes wider from 5 μm to 10 μm, then to 15 μm, with the morphology changing from clearly twisted, to straighter with small bulging instability, then to straighter with large bulging instability on both sides, respectively. Figure 8e shows that most AgNws are generally oriented along the print direction except some AgNws with deviated orientation. In Figure 8g, the AgNws wire with 10 μm PDS is about 1.1 μm high, and about 15 μm wide. It means the AgNws wires lost the height-width ratio of the initial frozen structure and tend to spread on the substrate, which is very different from the other two nanoparticles.

Figure 8f presents the deductive schematics of the release details of AgNws suspensions during sublimation. As an anisotropic nanomaterial, AgNws in the concentrated suspensions are also oriented along the ice/liquid interface during freezing as shown in Figure S12b. However, as 1D material, AgNws have two degrees of freedom along the ice/liquid interface. During sublimation, the AgNws will also be oriented along the surface of the shrinking frozen structure by the liquid capillary retract force, and remain two degrees of freedom along the surface plane, as shown in the upper inset in Figure 8f. Since AgNws have a large aspect ratio, according to Onsager theory,[25] [28] to make the final printed wire more ordered, more glycerol is required to maximize excluded volume effects between nanowires. The optimized AgNws+G0.4 ink has the largest volume ratio of 16.7 between glycerol and nanomaterials comparing with 0.6 of PS+G1.2 ink, 10.5 of GO+G1.8 ink. Therefore, the height-width ratio of the remain suspensions after sublimation is low as shown in Figure 8g.

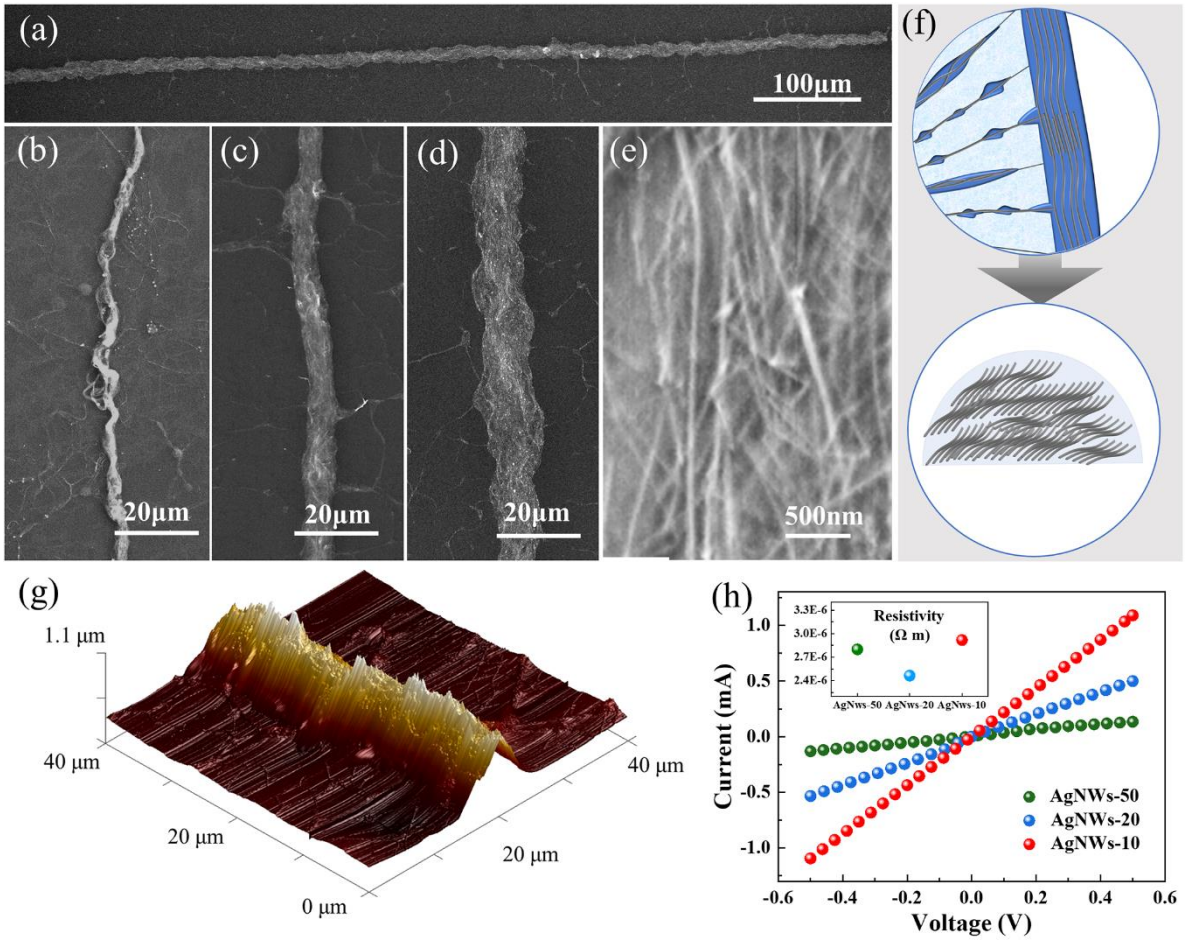

Figure 8. SEM images of AgNws wires with PDS of (a, d, and e) 50 μm, (b) 20 μm and (c) 10 μm, respectively. (f) Deductive schematics of release details of AgNws suspensions during sublimation. (g) AFM image and (h) I–V curves and resistivities of the printed AgNws wires.

After vacuum drying, the AgNws samples were placed on a hotplate at 130 °C for 5 minutes. Figure 8h shows the I-V curves of the AgNws wires. The electrical conductivity increases with PDS decreasing. The resistances per unit length of AgNws-50 (50 μm PDS), AgNws-20 (20 μm PDS) and AgNws-10 (10 μm PDS) are 3.74, 1.00 and 0.46 kΩ mm^{-1}, respectively. The resistivities measured according to Equation S1 and the cross-sectional area (Figure S14b) of the printed AgNws wires are 2.8×10^{-6} Ω m, 2.5×10^{-6} Ω m and 2.9×10^{-6} Ω m, respectively, which are low enough for the applications of microelectronic devices.

2.7 FSE-INS mechanism

From the results of the three kinds of nanoparticles, the FSE-INS mechanism can be described as following: Freezing induced the concentration of nanoparticle suspensions and limitation of drop spreading, and provided a good base to inhibit Rayleigh-Plateau instability for the next shrinking processes; sublimation gradually released the concentrated suspensions and provided a shrinking ice template carrying the suspensions on its surface shrinking together with inhibition of Rayleigh-Plateau instability, which is the main process for the small FS wires; the final evaporation made the structure after sublimation denser by capillary force. The mechanism not only realize microwires with small FS by inhibit Rayleigh-Plateau instability, but also keeps all the advantages of inkjet technology, including digital, as shown in Figure S13. Note that the mechanism can improve the print resolution at a certain extent, which is determined by the freezing induced drop spreading limitation. The plane property of the ice/liquid interface and the shrinking ice template make the FSE-INS mechanism particle-dimension dependent. By providing vertical solid surfaces on the substrate, the 2D materials in the released concentrated suspensions tend to be aligned vertically. Such vertically aligned 2D material structure is promising to build on-chip novel devices. We explored the 3D micropillar printing by the inks of PS nanoparticles in Figure S15-17 and GO nanosheets in Figure S18, respectively. The preliminary results show less or even no glycerol in the inks has bigger opportunity to realize 3D micropillar due to the suppressed downward flow of the released suspensions during sublimation. Considering the close packing property in vertical direction and high height-width ratio, 3D nanoparticles are more applicable to build 3D structures. However, without glycerol, the micropillars tend to be porous, although “porous” is also useful, e.g. sensors. To increase the density of 3D micropillar, the solvent provides both capillary bridges and suppression of downward flow during sublimation needs to be developed. It is meaningful to note that FSE-INS mechanism creates sacrificial vertical structure, which introduces an additional freedom to manipulate the nanoparticle arrangement perpendicular to the horizontal substrate plane, and is very different from conventional vertical direction inkjet printing method by droplet solidification by thermal or UV curing.[29] Note that thermal curing will decrease reliability of printhead, while UV curing will introduce sometimes unnecessary UV resin in the structures. Beside the nanoparticle-level structure manipulation along the

sacrificial vertical solid surfaces, the droplet-level structure manipulation along vertical direction by FSE-INS mechanism is also very useful. In general, the FSE-INS mechanism provides many freedoms to manipulate nanoparticles, which exhibits great potential to build novel devices.

3. Conclusion

In conclusion, the research in this paper was motivated by inkjet 3D printing microwires with small FS, and without sacrificing the advantages of inkjet technology. We successfully printed PS colloidal particles, GO, and AgNws microwires with small FS by FSE-INS mechanism. GO wire achieves the minimum FS of 2 μm among all the wires. We found this mechanism was particle-dimension dependent, and introduced sacrificial vertical solid surfaces which is an additional particle manipulation freedom perpendicular to the substrate, and provides an efficient way for on-chip integration of novel microelectronic devices and 3D structures with small FS, and fully utilizing of the advantages of inkjet technology.

4. Experimental Section

Materials: Monodisperse polystyrene (PS) colloidal nanoparticles dispersions (mean size~210nm) were purchased from Tianjin BaseLine ChromTech Research Center. Graphene oxide (GO) dispersions (No: XF020-100075, nanosheet diameter < 500 nm, C/O = 1.94) were purchased from Nanjing XFNANO Materials Tech Co., Ltd.. AgNws dispersions (diam. × L 20 nm (±2 nm) × 12 μm (±2 μm)) were purchased from Sigma-Aldrich. TBA was purchased from Sanen Chemical Technology (Shanghai) Co., Ltd.. Glycerol was purchased from Sinopharm Chemical Reagent Co., Ltd.

Ink preparation：Inks were prepared by adding 20 wt% TBA into PS/GO/AgNws water dispersions, respectively. Four kinds of PS inks with 1.5 wt% PS nanoparticles were prepared with glycerol of 0, 0.6, 1.2, and 1.5 wt%, and named as PS+G0, PS+ G0.6, PS+G1.2, and PS+G1.5, respectively. Five kinds of GO inks with 0.3 wt% GO nanosheets were prepared with glycerol of 0, 0.6, 1.2, 1.8, and 2.4 wt%, and named as GO+G0, GO+G0.6, GO+G1.2, GO+G1.8, and GO+G2.4, respectively. The optimized AgNws ink with 0.2 wt% AgNws was

prepared with 0.4 wt% glycerol, and named as AgNws+G0.4.

Printing Conditions: The inks were printed by a SciZntics3 Microelectronic printer (Shanghai Mifang Electronic Technology Co., Ltd.) with 10 pL printhead (FujiFilm Dimatix DMC-11610) and 21 μm nozzle diameter. A double-pulse waveform (Fig. S1a) for low surface tension and low viscosity inks was used to effectively reduce satellite drops. The wires were printed by 20 passes on silicon (001) substrate, with frequencies of 200 Hz, 500 Hz, and 1000Hz, respectively. The substrate was cooled at -40 °C by an ultra-high precision low-temperature thermostat bath.

Droplet freezing process imageing： Since the nozzle plate of the dimatix printhead is only about 2 mm distance to the substrate, and the nozzles are at the center of the square printhead surface plane, there is no space to observe the droplet behavior on substrate. To provide enough space to clear observe the droplet freezing process during printing, a single-nozzle glass-tube-type microfab printhead with the nozzle size of 30 μm (purchased from Shanghai Ruidu Photoelectric Technology Co., Ltd.) was used. The distance between nozzle and substrate is also about 2mm. PS+G1.2 ink was used for the imaging. A three-axis displacement table was used to control the movement of the printhead, and the jetting waveform and frequency were controlled by a microfab controller. A long-focus optical microscope was mounted with 45° to the substrate to observe the droplet freezing process during printing. Videos were recorded by a CCD camera.

Polarizing microscope imaging: A self-build polarizing microscope with CCD camera and two polarizing plates was used for imaging. The liquids to be measured were dropped between two slides. Then the two slides with liquid between them were put into the lyophilizer for 1 hour to ensure the liquid fully frozen. Finally, the frozen samples were taken out and imaged by polarizing microscope. During measurement, the upper surface of slide surface was cleaned with alcohol.

Sublimation process observation: A long-focus optical microscope was mounted on the outside of the transparent cover of the lyophilizer (Scientz-12, Ningbo Scientz Biotechnology Co., Ltd.) to observe the sublimation process. Videos were recorded by a CCD camera.

Characterization: The structures of the printed wires were investigated by the scanning electron microscopy (SEM) (Quanta FEG 250, FEI, USA). The inks rheological properties were

measured by a rheometer (Kinexus Lab+, NETZSCH Instruments, UK). The surface tensions of the inks were measured by a surface tensiometer (QBZY, Fangrui Instrument, China). PS nanoparticle size distribution was measured by nanoparticle size analyzer (Zetasizer Nan, Malvern, UK). Differential Scanning Calorimeter (DSC250, TA instrument, USA) was used to measure the melting point of the frozen inks. Raman spectroscopy measurements of GO and rGO were performed by a Laser Confocal Raman Microspectroscopy (LABRAM HR, Horriba-JY, Japan). The I-V curves of RGO and AgNws samples were measured by digital Source Meter (KEITHLEY2400, USA). The reflection spectra of PS wires were measured by reflective optical microscope system (CX40, Fuxiang Optical, China).

Supporting Information

Supporting Information is available from the Wiley Online Library or from the author.

Acknowledgements

The authors gratefully acknowledge financial support by National Natural Science Foundation of China (No. 61575216), Key R&D programs in Jiangsu (No. BE2017082), R&D Plan for Key Areas of Guangdong Province (No. 2018B090905002) and Suzhou Science and Technology Program (No. SYG201850).

References

[1] a) H. Ali-Boucetta, K. T. Al-Jamal, K. Kostarelos, in *Biomedical Nanoetechnology: Methods and Protocols*, Vol. 726 (Ed: S. J. Hurst) **2011**, p. 299; b) K. J. Baeg, M. Caironi, Y. Y. Noh, *Advanced Materials* **2013**, 25, 4210; c) D. McManus, S. Vranic, F. Withers, V. Sanchez-Romaguera, M. Macucci, H. Yang, R. Sorrentino, K. Parvez, S.-K. Son, G. Iannaccone, K. Kostarelos, G. Fiori, C. Casiraghi, *Nat. Nanotechnol.* **2017**, 12, 343; d) L. Cheng, J. J. Liu, X. Gu, H. Gong, X. Z. Shi, T. Liu, C. Wang, X. Y. Wang, G. Liu, H. Y. Xing, W. B. Bu, B. Q. Sun, Z. Liu, *Advanced Materials* **2014**, 26, 1886; e) A. Klestova, N. Cheplagin, K. Keller, V. Slabov, G. Zaretskaya, A. V. Vinogradov, *Advanced Optical Materials* **2019**, 7; f) A. Samusjew, M. Kratzer, A. Moser, C. Teichert, K. K. Krawczyk, T. Griesser, *Acs Applied Materials & Interfaces*

2017, 9, 4941.

[2] B. Derby, *Annual Review of Materials Research* **2010**, 40, 395.

[3] a) L. Wu, Z. Dong, M. Kuang, Y. Li, F. Li, L. Jiang, Y. Song, *Advanced Functional Materials* **2015**, 25, 2237; b) S. Chen, M. Su, C. Zhang, M. Gao, B. Bao, Q. Yang, B. Su, Y. Song, *Advanced Materials* **2015**, 27, 3928.

[4] a) Y. Zhang, B. Zhu, Y. Liu, G. Wittstock, *Nature Communications* **2016**, 7; b) Y. Zhang, D. Li, Y. Liu, G. Wittstock, *Small* **2018**, 14, 1801212.

[5] H. Abdolmaleki, P. Kidmose, S. Agarwala, *Advanced Materials* **2021**, 33, 2006792.

[6] J. Hou, M. Li, Y. Song, *Angewandte Chemie International Edition* **2018**, 57, 2544.

[7] G. Boussinot, E. A. Brener, *Phys Rev E Stat Nonlin Soft Matter Phys* **2015**, 92, 032408.

[8] R. Abbel, P. Teunissen, J. Michels, W. A. Groen, *Advanced Engineering Materials* **2015**, 17, 615.

[9] J. Attwater, A. Wochner, V. B. Pinheiro, A. Coulson, P. Holliger, *Nature Communications* **2010**, 1, 76.

[10] a) H.-Y. Tung, Z.-Y. Guan, T.-Y. Liu, H.-Y. Chen, *Nature Communications* **2018**, 9, 2564; b) E. Jambon-Puillet, N. Shahidzadeh, D. Bonn, *Nature Communications* **2018**, 9, 4191.

[11] a) K. Furukawa, S. Shibuta, K. Judai, *Journal of Molecular Liquids* **2020**, 319, 114170; b) J. Gliński, G. Chavepeyer, J. K. Platten, *The Journal of Chemical Physics* **1995**, 102, 2113.

[12] D. Ying, Z. Wang, Y. Zheng, J. Cai, L. Zhang, *Macromolecular Rapid Communications* **2021**, 42, 2000502.

[13] T. Chang, G. Zhao, *Advanced Science* **2021**, 8, 2002425.

[14] a) J. R. Castrejon-Pita, K. J. Kubiak, A. A. Castrejon-Pita, M. C. T. Wilson, I. M. Hutchings, *Phys. Rev. E* **2013**, 88, 11; b) J. Blake, D. Thompson, D. Raps, T. Strobl, *Aiaa J.* **2015**, 53, 1725; c) J. E. Castillo, Y. B. Huang, Z. H. Pan, J. A. Weibel, *Int. J. Heat Mass Transf.* **2021**, 164, 13.

[15] a) Y. Suzuki, S. Takeya, *The Journal of Physical Chemistry Letters* **2020**, 11, 9432; b)

W. Zhu, C. Zhang, Y.-d. Zhu, R. An, X.-h. Lu, Y.-j. Shi, S.-y. Jiang, *Journal of Molecular Liquids* **2019**, 291, 111238; c) Y. Suzuki, *Journal of Chemical Physics* **2020**, 152; d) Y. Hayashi, A. Puzenko, Y. Feldman, *Journal of Non-Crystalline Solids* **2006**, 352, 4696.

[16] a) S. S. L. Peppin, J. A. W. Elliott, M. G. Worster, *Journal of Fluid Mechanics* **2006**, 554, 147; b) S. Deville, in *Freezing Colloids: Observations, Principles, Control, and Use: Applications in Materials Science, Life Science, Earth Science, Food Science, and Engineering*, DOI: 10.1007/978-3-319-50515-2_3 (Ed: S. Deville), Springer International Publishing, Cham **2017**, p. 91.

[17] B. S. Bhatnagar, J. Sonje, E. Shalaev, S. W. H. Martin, D. L. Teagarden, R. Suryanarayanan, *Physical Chemistry Chemical Physics* **2020**, 22, 1583.

[18] K. Kasraian, P. P. DeLuca, *Pharmaceutical Research* **1995**, 12, 484.

[19] a) D. J. Hornbaker, R. Albert, I. Albert, A. L. Barabási, P. Schiffer, *Nature* **1997**, 387, 765; b) M. Scheel, R. Seemann, M. Brinkmann, M. Di Michiel, A. Sheppard, B. Breidenbach, S. Herminghaus, *Nature Materials* **2008**, 7, 189; c) S. Strauch, S. Herminghaus, *Soft Matter* **2012**, 8, 8271.

[20] a) T. T. B. Nguyen, S. Mitra, M. J. Sathe, V. Pareek, J. B. Joshi, G. M. Evans, *Experimental Thermal and Fluid Science* **2018**, 91, 329; b) T. T. B. Nguyen, S. Mitra, V. Pareek, J. B. Joshi, G. M. Evans, *Experimental Thermal and Fluid Science* **2018**, 99, 558.

[21] K. Ueno, Y. Sano, A. Inaba, M. Kondoh, M. Watanabe, *The Journal of Physical Chemistry B* **2010**, 114, 13095.

[22] a) S. Saleh Mohammad, C. Hu, R. Panat, *Science Advances* 3, e1601986; b) F. Zheng, Z. Wang, J. Huang, Z. Li, *Microsystems & Nanoengineering* **2020**, 6, 89.

[23] Y. I. Rabinovich, M. S. Esayanur, B. M. Moudgil, *Langmuir* **2005**, 21, 10992.

[24] R. Jalili, S. H. Aboutalebi, D. Esrafilzadeh, K. Konstantinov, J. M. Razal, S. E. Moulton, G. G. Wallace, *Materials Horizons* **2014**, 1, 87.

[25] a) L. Shi, Y. Zhang, B. Dong, T. Zhan, X. Liu, J. Zi, *Advanced Materials* **2013**, 25, 5314; b) X. Wang, L. Wu, G. Wang, G. Chen, *Nano Letters* **2019**, 19, 8225.

[26] R. Jalili, S. H. Aboutalebi, D. Esrafilzadeh, R. L. Shepherd, J. Chen, S. Aminorroaya-Yamini, K. Konstantinov, A. I. Minett, J. M. Razal, G. G. Wallace, *Advanced Functional Materials* **2013**, 23, 5345.

[27] I. K. Moon, J. Lee, R. S. Ruoff, H. Lee, *Nature Communications* **2010**, 1, 73.

[28] A. Rawal, *Mechanics of Materials* **2021**, 160, 103901.

[29] a) P. V. Shinde, R. Samal, C. S. Rout, *Advanced Materials Interfaces* **2022**, 9, 2101959; b) J. Alamán, M. López-Valdeolivas, R. Alicante, J. I. Peña, C. Sánchez-Somolinos, *Polymers (Basel)* **2019**, 11, 430.